ADVANCED MATERIALS
www.advmat.de

Counter-Doping Effect by Trivalent Cations in Tin-Based Perovskite Solar Cells

*Tianyue Wang, Hok-Leung Loi, Qi Cao, Guitao Feng, Zhiqiang Guan, Qi Wei, Changsheng Chen, Mingjie Li, Ye Zhu, Chun-Sing Lee, and Feng Yan**

Tin (Sn) -based perovskite solar cells (PSCs) normally show low open circuit voltage due to serious carrier recombination in the devices, which can be attributed to the oxidation and the resultant high p-type doping of the perovskite active layers. Considering the grand challenge to completely prohibit the oxidation of Sn-based perovskites, a feasible way to improve the device performance is to counter-dope the oxidized Sn-based perovskites by replacing Sn^{2+} with trivalent cations in the crystal lattice, which however is rarely reported. Here, the introduction of Sb^{3+}, which can effectively counter-dope the oxidized perovskite layer and improve the carrier lifetime, is presented. Meanwhile, Sb^{3+} can passivate deep-level defects and improve carrier mobility of the perovskite layer, which are all favorable for the photovoltaic performance of the devices. Consequently, the target devices yield a relative enhancement of the power conversion efficiency (PCE) of 31.4% as well as excellent shelf-storage stability. This work provides a novel strategy to improve the performance of Sn-based PSCs, which can be developed as a universal way to compensate for the oxidation of Sn-based perovskites in optoelectronic devices.

1. Introduction

Organic–inorganic metal halide perovskite solar cells (PSCs) have aroused tremendous research interest as the next-generation photovoltaic technology due to their high efficiency and facile fabrication processes.[1–6] However, high-performance PSCs are typically based on lead halide perovskites with bandgaps at ≈1.5–1.6 eV, which exceed the ideal range (1.1–1.4 eV) according to the Shockley-Queisser limit for a single-junction solar cell.[7] Besides, the high toxicity of lead also limits the practical application of PSCs.[8,9] Notably, pure tin (Sn) -based perovskites are the most promising candidates for the development of lead-free PSCs because of their lower bandgap energy and environmentally friendly nature.[10–12] Since 2020, notable advancements have been achieved in the realm of Sn -based PSCs, wherein their efficiency has surpassed the threshold of 14%.[13–23] However, the pace of progress has considerably decelerated recently. A key issue lies in the fact that Sn-based PSCs suffer from significant carrier recombination within the active layer, which creates a big gap between the real photovoltaic parameters, such as power conversion efficiency (PCE), open-circuit voltage (V_{OC}) and fill factor (FF), and the full thermodynamic potential.[24,25] The primary causative factor has been ascribed to the inherent susceptibility of Sn-based perovskites to oxidation even in a controlled environment such as a glovebox with Sn^{2+} converted to Sn^{4+}.[25–29] As a result, a high density of tin vacancies forms in the bulk, causing unintentional background p-type doping for a photovoltaic device.[30,31]

For Sn-based PSCs, the doping levels in perovskite layers have been characterized by several groups, mainly ranging from 10^{16}–10^{19} cm^{-3} (Table S1, Supporting Information), which are much higher than that in a lead-based PSC. The highly doped Sn-based perovskites have a high charge-carrier recombination rate under light illumination due to both monomolecular and bimolecular recombination.[30,32,33] For example, Milot et al. reported a radiative monomolecular charge recombination pathway in $FASnI_3$ due to high p-type doping in the bulk, leading to decreased carrier lifetimes and suppressed carrier transport in the thin film.[33] On the other hand, high p-type doping up to 10^{19} cm^{-3} in the perovskite film of a PSC may result in a narrow depletion width down to several nanometers at the junction with the electron transporting layer, which allows electron tunneling at the junction and gives rise to a high reverse saturation current in the device. According to the diode equation, the V_{OC} of a PSC

T. Wang, H.-L. Loi, Q. Cao, G. Feng, Q. Wei, C. Chen, M. Li, Y. Zhu, F. Yan
Department of Applied Physics
The Hong Kong Polytechnic University
Hung Hom, Kowloon, Hong Kong SAR 999077, P. R. China
E-mail: apafyan@polyu.edu.hk
Z. Guan, C.-S. Lee
Center of Super-Diamond and Advanced Films (COSDAF)
Department of Chemistry
City University of Hong Kong
Kowloon Tong, Hong Kong SAR 999077, P. R. China
F. Yan
Research Institute of Intelligent Wearable Systems
The Hong Kong Polytechnic University
Hung Hom, Kowloon, Hong Kong SAR 999077, P. R. China

The ORCID identification number(s) for the author(s) of this article can be found under https://doi.org/10.1002/adma.202402947

DOI: 10.1002/adma.202402947

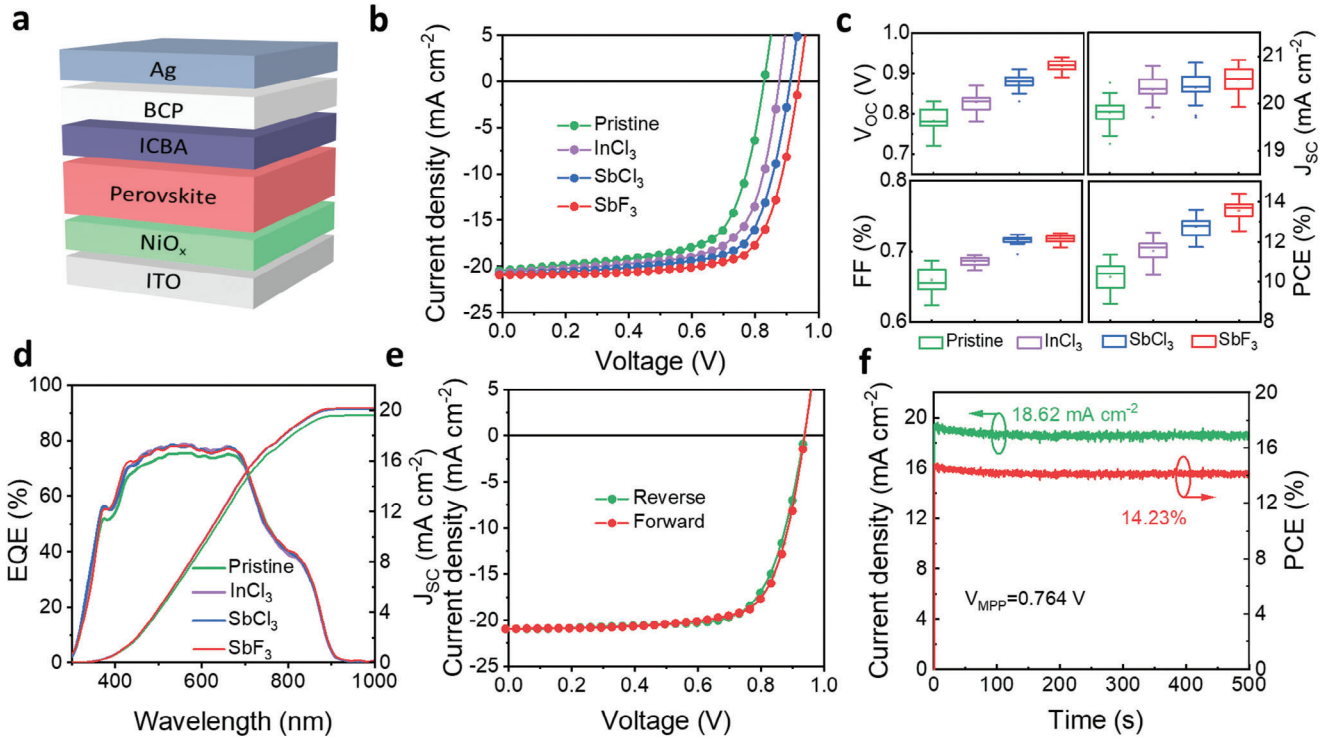

Figure 1. a) Schematic illustration of the device structure of Sn-based PSCs. b) The *J-V* curves of the best-performed devices with the pristine perovskite and perovskites doped with $InCl_3$, $SbCl_3$, and SbF_3 at an optimized molar ratio of 0.015%, 0.01%, and 0.01% respectively under forward scan directions. c) V_{OC}, J_{SC}, FF, and PCE statistics of PSCs of each condition. d) EQE spectra and integrated J_{SC} of the pristine and trivalent metal halides doped PSCs. e) The *J-V* curves of the best-performed SbF_3-doped devices under both the reverse (green circle) and forward (red circle) scan directions. f) The stabilized power output for the champion SbF_3-doped device.

is given by: $V_{oc} = \frac{nkT}{q} ln(\frac{J_{sc}}{J_0} + 1)$, where n is the ideality factor, J_{sc} is the photogenerated short-circuit current density, J_o is the reverse saturation current density of the device, k is the Boltzmann constant and T is temperature.[34] As addressed above, high p-type doping in Sn-based perovskites can lead to high J_o of resultant PSCs due to high charge-carrier recombination rates and tunneling currents, thus generating low V_{OC} of the devices. Indeed, highly doped Sn-based PSCs all show much higher Voc loss than Pb-based PSCs, as demonstrated in Table S1 (Supporting Information). To alleviate the adverse impacts of p-type doping, several approaches have been extensively studied, such as the introduction of additives, control of material morphology, surface passivation, and manipulation of lattice dimensionality.[35] Another alternative approach involves the introduction of dopants with opposite charge carriers, referred to as counter-doping, however, has received limited attention in previous studies.

In this study, we employed 2D–3D mixed Sn halide perovskite with a composition of $PEA_2FA_{n-1}Sn_nI_{3n+1}$ (n = 10) in PSCs. To counter-dope the unintended self-p-type doping in Sn-based perovskite, which arises from Sn^{2+} vacancies, we opted to substitute Sn^{2+} cations with trivalent cations (i.e., Sb^{3+} and In^{3+}). Interestingly, the doping level in the Sn-based perovskite was decreased substantially down to 10^{14} cm^{-3} by adding a tiny amount of SbF_3, leading to an increase of V_{OC} and FF of the PSC. To better understand the underlying mechanism, the counter-doping effect was characterized systematically. We found that Sb^{3+} substitution at the Sn^{2+} site could upshift the Fermi level of perovskite toward the conduction band by contributing free electrons, which effectively suppresses the background hole density. Additionally, the incorporation of Sb^{3+} could convert deep-level defects induced by iodine vacancies into shallow-level defects, thus extending carrier lifetimes and transport properties in perovskite films. Our strategy boosts the performance of Sn-based PSCs with an enhancement of 31.4% in their PCE. The champion device shows a PCE of 14.37% and a V_{OC} of 0.938 V. The SbF_3 doped device also exhibits excellent long-term stability, which retains 95% of the initial PCE after storage in N_2 -filled glovebox for more than 1500 h.

2. Results and Discussion

As illustrated in **Figure 1a**, Sn-based PSCs were fabricated with an inverted cell architecture of ITO/NiO_x/perovskite/ICBA/BCP/Ag. To improve the device performance, three different additives, including indium (III) chloride ($InCl_3$), antimony(III) chloride ($SbCl_3$), and antimony(III) trifluoride (SbF_3), were introduced in the perovskite precursor solutions with different percentages. As shown in Figure S1 (Supporting Information), as the concentration ratio of SbF_3 increases at a molar ratio from 0% to 0.03%, the average PCE is enhanced from 10.22% to 13.55% at an optimal SbF_3 ratio of 0.01%, then it drops to 6.86%, with significantly reduced V_{OC} and J_{SC}. Notably, too high Sb-doping may lead to a higher carrier recombination

rate, which will be made clear in the following experiments, and consequently degraded photovoltaic performance. Considerable PCE improvements were also obtained with $SbCl_3$ and $InCl_3$ doping at an optimized concentration ratio of 0.01% and 0.015%, respectively, as shown in Figure S1 (Supporting Information). In the following discussion, if not otherwise mentioned, the doping ratio of different additives denotes the optimum.

Figure 1b shows the *J-V* curves of the best-performed PSCs under forward *J-V* scan conditions. The pristine device gives a J_{SC} of 20.44 mA cm^{-2}, V_{OC} of 0.830 V, FF of 66.84%, and a PCE of 11.34%. Trivalent metal halide doping results in a large increase of the V_{OC} and FF, and thus enhances the device PCE. Among them, SbF_3 doped PSC yields the best PCE of 14.37%, with a J_{SC} of 20.92 mA cm^{-2}, V_{OC} of 0.938 V, and FF of 73.23%. The statistical data of 15 individual cells for each condition as shown in Figure 1c further verifies the reproducibility of the performance enhancement. Notably, SbF_3-doped devices yield a relative enhancement of the PCE of 31.4%. The integrated J_{SC} for the pristine, $InCl_3$, $SbCl_3$, and SbF_3 doped PSCs from their external quantum efficiency (EQE) spectra are 19.61, 20.09, 20.12, and 20.22 mA cm^{-2}, respectively (Figure 1d), agreeing well with the values from *J-V* curves (Figure 1b). The improvement of J_{SC} with trivalent metal halide doping is comparatively insignificant concerning the increase in V_{OC} and FF, given that the absorption of perovskite films almost remains unaltered (Figure S2, Supporting Information). Importantly, the best-performing PSC doped with SbF_3 exhibits a negligible hysteresis in *J-V* curves, generating a PCE of 14.37% and 14.12% respectively from forward and reverse scans (Figure 1e). We further measured the photocurrent density of the device at the bias of 0.764 V, the maximum output power point (MPPT), for a certain period (Figure 1f). A stabilized efficiency of 14.23% is obtained after 500 s, which is close to the result presented in Figure 1e.

To better understand the mechanism of trivalent metal halide doping, we systematically examine their effects on the optoelectronic properties and morphologies of Sn-based perovskite films. The introduction of the optimal amount of trivalent metal halide additive does not cause any noticeable change to the absorption spectra, and a bandgap of 1.40 eV can be determined from the extracted Tauc plots (Figure S2, Supporting Information). The top-view scanning electron microscopy (SEM) images for all the samples show a surface morphology that is flat, smooth, and fully covered, with grain boundaries that are almost fused (Figure S3, Supporting Information). To better characterize the perovskite film properties, we exfoliated the films from ITO/NiO_x substrates using a UV-curable resin to visualize the buried interfaces (Figure S4, Supporting Information). The experimental details can be found in Note 1 (Supporting Information). We observe the presence of potholes on the pristine film, which contributes to its overall uneven surface. $SbCl_3$ and SbF_3 doped films exhibit slightly reduced potholes than the pristine and $InCl_3$ doped films, probably due to the fact that the exotic Sb^{3+} ion changes the surface energy of the crystal growth front and impacts the film formation kinetics.[36] The effect of antimony halide doping on morphology optimization is favorable for PSC performance enhancement. Moreover, the introduction of SbF_3 dopant in Sn-based PSC results in a slightly increased efficiency in comparison to $SbCl_3$. The differential impact of SbF_3 and $SbCl_3$ additives primarily stems from the variance in their respective anions. F^- is a smaller anion with greater electronegativity (3.98) than Cl^- (3.16), showing a stronger affinity for the adjacent Sn^{2+} on the surface of the perovskite lattice, which is expected to passivate undercoordinated Sn^{2+} defects and also prevent Sn^{2+} species from losing their electron pair in further oxidation.[37,38] The character of F^- is also employed in a previous work to stabilize the lead halide perovskite surface via increased bonding with Pb^{2+} to suppress vacancy formation.[39]

X-ray diffraction (XRD) measurements were performed on the resultant films to elucidate their lattice structures. XRD peaks at 3.5720° (corresponding to the n = 2 2D phase) and 14.0032° (corresponding to the (100) plane of 3D phase) slightly shift toward higher 2θ degrees with trivalent metal halide doping (Figure S5, Supporting Information), indicating the shrinkage of the lattice of 2D–3D mixed Sn halide perovskites. Due to the significant difference in ionic radii between I^- and Cl^- or F^-, there are scarcely any reports of Cl^- and F^- doping into the Sn halide perovskite lattice.[26,40] Thus the lattice shrinkage can be rationalized through the substitution of some Sn^{2+} (96 pm) sites by Sb^{3+} (76 pm) or In^{3+} (80 pm) ions with smaller ionic radius.[41] The substitution of trivalent cations on Sn^{2+} sites is expected to lead to a counter-doping effect in p-type Sn halide perovskite films. Given the biggest performance enhancement induced by SbF_3, we then investigate its doping effect systematically in the following experiments.

To probe the regions affected by SbF_3 doping, we performed depth profiling of Sn perovskite films using time-of-flight secondary-ion mass spectroscopy (ToF-SIMS). As shown in **Figure 2a**, the signal of Sb^+ can be detected throughout the Sn perovskite film, in accordance with a homogeneous doping profile. Additionally, the homogeneous distribution of Sb^+ in the bulk of Sn perovskite film can be observed more clearly from the 3D distribution image, as shown in Figure S6 (Supporting Information). To investigate the chemical composition and ion interaction of the perovskite film with SbF_3 doping, we performed X-ray photoelectron spectroscopy (XPS) characterization. Notably, measurements were carried out after surface etching of the films for 10 s to remove the surface oxidant and contamination. The perovskite films were modified with 0.1% SbF_3 exceeding the optimal amount due to the detection limit of XPS. The result in Figure S7 (Supporting Information) indicates the presence of Sb^{3+} in the perovskite film. The Sn 3d and I 3d spectra are also shown in Figure 2b,c. Both the Sn 3d and I 3d core levels shift to higher binding energy upon SbF_3 introduction, indicative of a shift in the Fermi level toward the conduction band.[42,43] It is possible that Sb^{3+} is incorporated into the perovskite lattice, which produces an extra electron and thus changes the surrounding electron cloud density (Figures S8 and S9, Supporting Information).[44]

Further experimental measurements were conducted to investigate how SbF_3 doping impacts the electrical properties of Sn perovskite films. We first conducted hall-effect measurements to determine the doping type and level of Sn perovskite films without or with SbF_3 doping at room temperature. As shown in Figure 2d, all films exhibit a p-type doping behavior. The hole concentration (p) of the pristine film is $\approx 1.79 \times 10^{16}$ cm^{-3}, which decreases with the increase of the Sb^{3+} doping ratio. Notably, the addition of 0.01% SbF_3 can significantly reduce hole concentration to $\approx 6.46 \times 10^{14}$ cm^{-3} in the perovskite sample

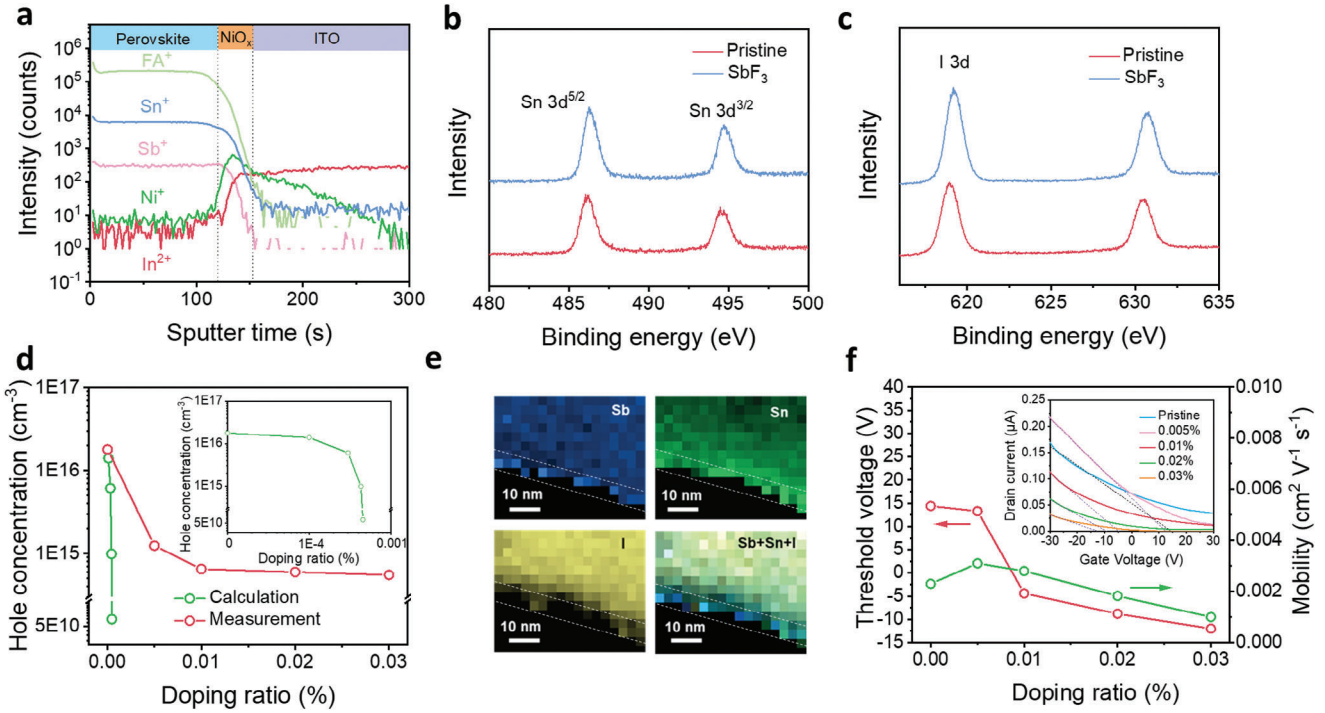

Figure 2. a) ToF-SIMS depth profile of Sb ion in SbF_3 modified perovskite film deposited on NiO_x/ITO. XPS Sn 3d core-level spectra (b) and I 3d core-level spectra (c) of pristine and SbF_3 doped perovskite films. d) Theoretical and measured hole concentrations of SbF_3 doped- perovskite films at varied doping ratios as determined from hall characterizations. Inset: magnified theoretical hole concentrations of SbF_3 doped- perovskite films at varied doping ratios. e) STEM-HAADF image of a perovskite grain and the STEM−EELS maps of Sb, Sn, and I as well as the superposition of the elements corresponding to 0.01% SbF_3 doped perovskite film. The region between two dash lines corresponds to the grain surface. f) Calculated threshold voltage and mobility from transfer curves of field-effect transistors (see inset in (f)) prepared by depositing the pristine and SbF_3 doped perovskite films at varied concentrations on SiO_2/Si substrates. $V_D = 0.5$ V.

while a further increase of SbF_3 doping to 0.03% only lead to a slightly decreased hole concentration of 5.51×10^{14} cm^{-3} and n-type perovskite films have never been achieved even at higher addition levels of SbF_3. As a result, the conductivity (σ) is also dramatically decreased by about an order of magnitude in 0.01% SbF_3 doped film. Additionally, the hall mobility of holes ($\mu_h = \sigma$/pe) is observed to increase with a higher doping ratio, which is advantageous to carrier transport within the perovskite film (Figure S10, Supporting Information). Besides, we have calculated the hole concentration in the pristine perovskite film as a function of the doping ratio of SbF_3 assuming that Sb^{3+} cations are all incorporated in the crystal lattice. Given that $FASnI_3$ crystal has an orthorhombic unit cell and lattice parameters of a = 6.3286 Å, b = 8.9554 Å, and c = 8.9463 Å,[45] the doping ratio of ≈0.0005 mol% can completely counter-dope the p-type film to intrinsic, as shown in the inset in Figure 2d. Therefore, only part of Sb^{3+} cations have been involved in counter-doping Sn-based perovskites in the crystal lattice. Indeed, the segregation of excess Sb^{3+} cations at perovskite grain boundaries has been observed under scanning transmission electron microscopy (STEM) with the function of electron energy loss spectra (EELS). Besides, the incorporation of Sb^{3+} inside the perovskite grain has been observed as well (Figure 2e; Figure S11, Supporting Information). Hence, we conclude that only partial Sb^{3+} cations can counter-dope p-type Sn perovskite films effectively.

To understand the mechanism behind the partial participation of Sb^{3+} cations in the counter-doping process of Sn-based perovskites, the formation energies ($\Delta E[Sb_{Sn}]$) of Sb^{3+} incorporated perovskites were calculated according to first-principal density functional theory (DFT) (see Supporting Information). As shown in Figure S9b and S12b (Supporting Information), $FA_8Sn_7Sb_1I_{24}$ and $FA_{64}Sn_{63}Sb_1I_{192}$ supercells were created, corresponding to a substantial doping concentration of Sb^{3+} and a comparatively lower doping concentration into the lattice, respectively. $\Delta E[Sb_{Sn}]$ of $FA_8Sn_7Sb_1I_{24}$ is 0.95 eV, higher than that of $FA_{64}Sn_{63}Sb_1I_{192}$ (0.48 eV) and perfect perovskite supercell (0 eV) (Table S2, Supporting Information). A higher $\Delta E[Sb_{Sn}]$ means that substituting a significant amount of Sn^{2+} with Sb^{3+} can result in lattice instability. Additionally, according to the results of formation energies of $FA_{64}Sn_{63}Sb_1I_{192}$ at different charge states and corresponding charge transition energy levels, Sb^{3+} substitution for Sn^{2+} induces shallow donor-like defect behavior in the perovskite film, which again confirms the role of Sb^{3+} in donating electrons (Figure S13, Supporting Information).[46,47] Given that the pristine perovskite film in the experiment is p-type induced by Sn vacancies, we also examine the formation energy ($\Delta E[Sb_{Sn}][V_{Sn}]$) of Sb^{3+} incorporated perovskite in the presence of Sn vacancies. Specifically, perovskite supercells of $FA_8Sn_6Sb_1I_{24}$ and $FA_{64}Sn_{62}Sb_1I_{192}$ were created with a Sn vacancy existing alongside a neighboring Sn^{2+} site substituted by Sb^{3+} (Figures S9d and S12c, Supporting Information).

$\Delta E[Sb_{Sn}][V_{Sn}]$ of $FA_8Sn_6Sb_1I_{24}$ and $FA_{64}Sn_{62}Sb_1I_{192}$ are −0.29 eV and −0.81 eV respectively, wherein a more negative value signifies an elevated propensity for Sb^{3+} to be doped into the lattice. Besides, the condition for a Sn vacancy existing along the diagonal direction of a Sn^{2+} site substituted by Sb^{3+} is also considered for $FA_{64}Sn_{62}Sb_1I_{192}$ supercell, which shows a $\Delta E[Sb_{Sn}][V_{Sn}]$ of −0.40 eV (Figure S12d and Table S2, Supporting Information). In essence, the absence of Sn vacancies within the perovskite crystal poses a significant challenge for the successful lattice doping of Sb^{3+} ions. However, when Sn vacancies are present, a minor fraction of Sb^{3+} doping is facilitated but the doping concentration in the crystal lattice should be less than the concentration of Sn vacancies. Nonetheless, this propensity is hindered when an excessive concentration of Sb^{3+} ions is introduced, resulting in their preferential residing on the grain surfaces. This accounts for the experimental finding that n-type Sn-based perovskite cannot be achieved by Sb^{3+} doping even at high SbF_3 addition levels. We further utilize Williamson-Hall analysis to investigate the doping effect of SbF_3 with varied concentrations. As the amount of SbF_3 increases from 0.01% to 0.03%, the microstrain in the film is significantly increased (Figure S14, Supporting Information), presumably due to the smaller atomic size of Sb^{3+} than Sn^{2+}, which distorts the crystal lattice. When the strain in polycrystalline perovskite increases to a certain extent, it can induce structural defects and consequently undesired non-radiative recombination, which decreases the V_{OC} of corresponding devices.[48,49]

Field effect transistors (FETs) were also fabricated to investigate the electronic properties of Sn perovskite films. We deposited films on Si/SiO_2 substrates and measured the drain current (I_D) versus gate voltage (V_G) curves, as shown in the inset in Figure 2f. The hole mobility (μ) and threshold voltage (V_{TH}) for different SbF_3 doping ratios are summarized in Figure 2f. The field-effect hole mobility is determined by:

$$\mu = \frac{dI_D}{dV_G} \cdot \frac{L}{W} \cdot \frac{1}{C_{ox} V_D} \quad (1)$$

where L, W, C_{ox} and V_D are the channel length, width, gate oxide capacitance per unit area and drain voltage, respectively. The increase in carrier mobility through SbF_3 doping can be attributed to the additive's ability to passivate defects, as demonstrated by the following DFT calculations. However, too much addition of SbF_3 (0.02% and 0.03%) decreases the carrier mobility due to the generation of trap states, which is consistent with the degraded photovoltaic performance at these doping levels. The V_{TH} is determined by linearly fitting I_D to V_G. The shift of V_{TH} to a lower gate voltage with the increase of SbF_3 concentration clearly indicates the counter-doping effect of Sb^{3+} in the perovskite films. Thus, the electronic properties of Sn-based perovskite films determined from FETs are consistent with those from hall-effect characterization.

Subsequently, ultraviolet photoelectron spectroscopy (UPS) was employed to investigate the energy band positions of Sn-based perovskite films. The Fermi levels (E_F) are −4.50, −4.33, −4.36, and −4.32 eV for the pristine, $InCl_3$, $SbCl_3$, and SbF_3 doped perovskite samples. The valence band (E_V) positions of pristine, $InCl_3$, $SbCl_3$, and SbF_3 doped perovskites are −5.06 eV, −5.03 eV, −5.05 eV, and −5.01 eV, respectively (**Figure 3**a,b; Figure S15, Supporting Information). The trivalent metal doping has led to the upshift of E_F of perovskite films, in agreement with the XPS results. Then we can draw the schematic energy band diagrams between the perovskite layer and NiO_x hole transport layer, as shown in Figure 3c,d and S15 (Supporting Information). The interface between NiO_x and pristine perovskite owns the smallest band offset of 0.04 eV, which is increased to 0.17 eV for the SbF_3 or $SbCl_3$ doped films (0.17 eV), and 0.18 eV for the $InCl_3$ doped film. The band offset of NiO_x/perovskite at ≈0.2 eV is preferably to provide a large built-in potential for the efficient separation of electrons and holes. Meanwhile, it is beneficial to reduce energy loss and promote hole transfer at the NiO_x/perovskite interface.

Photoluminescence (PL) measurements were carried out on Sn-based perovskite films to examine how trivalent metal doping impacts the film's optoelectronic properties. Figure S16 (Supporting Information) shows the steady-state PL spectra of perovskite samples. An increase in the PL intensity was observed with trivalent metal doping. Then, time-resolved photoluminescence (TRPL) was characterized for the samples, from which the average decay time constants (τ_{avg}) were determined to be 95.34 and 161.82 ns for the pristine and 0.01% SbF_3 doped samples, respectively (**Figure 4**a). The greatly enhanced PL intensity and prolonged τ_{avg} indicate a successful reduction of charge carrier recombination in perovskite thin films. Corresponding results involving $SbCl_3$ and $InCl_3$ can be found in Figure S16 and Table S3 (Supporting Information), where comparable deductions could likewise be made. However, the additions of SbF_3 at 0.02 and 0.03 mol% decrease the carrier lifetimes presumably due to the generation of more trap states in the perovskite films.

To have a quantitative assessment for the reduction of trap density with trivalent metal doping, space-charge limited current (SCLC) measurements were conducted based on electron-only devices with a structure of ITO/SnO_2/perovskite/ICBM/Ag. As shown in Figures 4b and S17 (Supporting Information), the trap-filled limit voltage (V_{TFL}) is 0.78 V for the pristine device, whereas it is decreased to 0.65 V for $InCl_3$ doped device, 0.53 V for $SbCl_3$ doped device, and 0.41 V for SbF_3 doped device. The number of defect densities (n_{trap}) can be calculated according to:

$$n_{trap} = \frac{2V_{TFL}\varepsilon\varepsilon_0}{qL^2} \quad (2)$$

where ε is the relative dielectric constant, ε_0 is the vacuum permittivity, q is the electron charge, and L is the perovskite film thickness. Accordingly, the trap density in Sn-based perovskite films is reduced from 5.47×10^{15} to 4.56×10,[15] 3.71×10^{15} and 2.87×10^{15} cm^{-3} with $InCl_3$, $SbCl_3$ and SbF_3 doping, respectively. This trend matches well with the PL results, indicating the effectiveness of trivalent metal doping in reducing the defects in Sn-based perovskite films. In addition, the decrease of trap density after the trivalent cations doping in this experiment can be attributed to the upshift of the Fermi level considering that traps beneath the Fermi level are filled with electrons already.

We further investigate the charge transfer and recombination processes in SbF_3 doped devices. To do so, dark J–V curves of PSCs were measured, as shown in Figure 4c. The PSC with SbF_3 doping exhibits a much lower reverse saturation current density due to less density of defects and lower leakage current in the device. Electrochemical impedance spectroscopy (EIS)

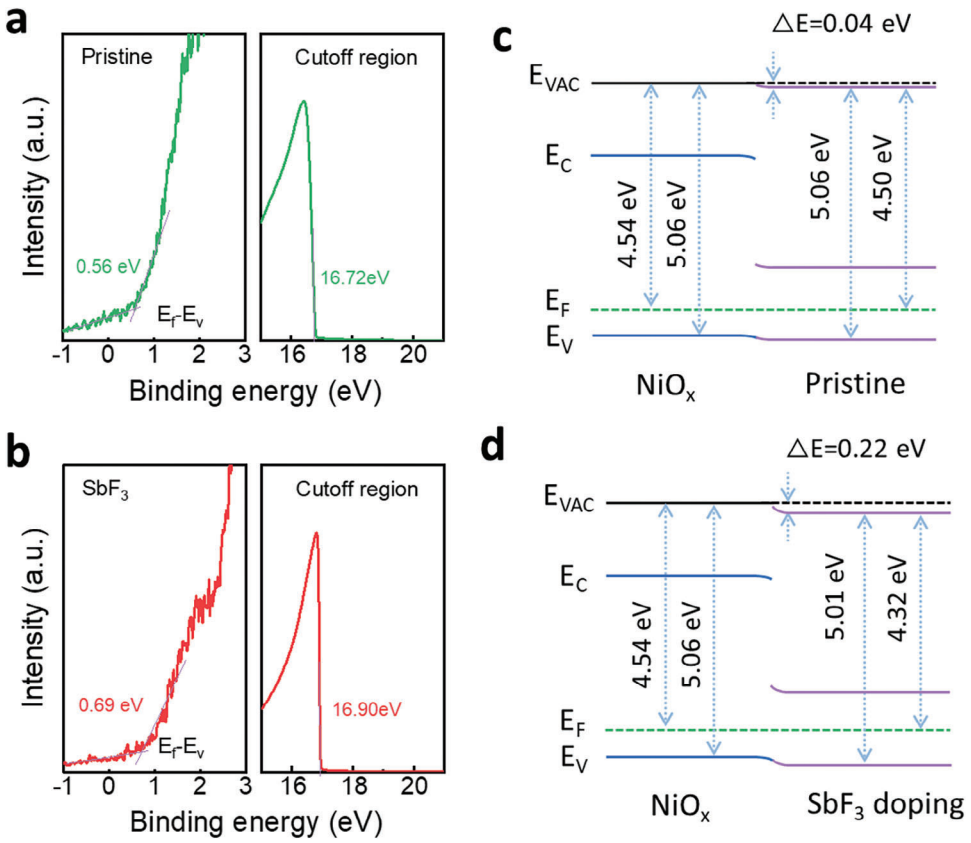

Figure 3. UPS spectra of the pristine (a) and SbF_3 doped (b) perovskite films. The schematic energy band diagrams between the NiO_x hole transport layer and the pristine perovskite layer (c) or SbF_3 doped perovskite layer (d).

characterizations were also performed for PSCs at a potential bias of 0.5 V. It can be found from Figure S18 (Supporting Information) that the Nyquist plots show semicircular curves, which can be fitted from the equivalent circuit model in the inset. Specifically, R_s is the series resistance, reflecting the carrier transport capability in the device, and R_{rec} is the recombination resistance, reflecting the charge recombination rate. The value of R_s is much smaller for SbF_3 doped PSC (38.37 Ω) compared to that of the pristine PSC (44.56 Ω), whereas R_{rec} has increased from 335.3 Ω for the pristine PSC to 840.1 Ω for SbF_3 -doped PSC (Table S4, Supporting Information), confirming restrained carrier recombination and improved charge transport in the device. The improvement of charge extraction in the device is also validated by Mott-Schottky analysis using capacitance-voltage (C-V) measurement. The SbF_3 doped device exhibits an enhanced V_{bi} from 0.63 to 0.70 V compared to the pristine device, which is beneficial for facilitating charge transport and improving the device V_{OC} (Figure 4d).

Furthermore, to assess the reduction of type of device defects, an admittance spectrum test was conducted (Figure 4e; Note 2, Supporting Information). The doping of SbF_3 can effectively reduce the density of deep energy level defects, which are considered the major source of non-radiative recombination in devices. The fact that the reduction in deep-level defects is also supported by PL and TRPL results. To gain insight into the defect passivation mechanism by SbF_3 additive, DFT calculations were performed. Due to the vulnerability of Sn perovskite crystal structure, inevitably, the ions (A-site cation, B-site cation, X-site anion) may deviate from the equilibrium sites and form a great number of point defects. Among various point defects, iodine vacancies (V_I) in pure Sn-based perovskites have been reported to act as deep donors (deep-level defects) with a high charge-state transition level, which is responsible for trap-mediated recombination. It is reported that the incorporation of other B-site cations can impact defect properties of V_I distinct from those of pristine perovskite.[46] We therefore suspect that the substitution of Sb^{3+} for Sn^{2+} plays a similar role. Defect calculations were performed in a 2 × 2 × 2 supercell of $FASnI_3$ perovskite for simplification, which is expected to mimic the property of 2D−3D mixed Sn halide perovskite since the interaction between Sb^{3+} and inorganic octahedron plays a key role. Figure S19a,b (Supporting Information) shows the perovskite supercell with a V_I defect and supercell with a V_I defect with Sb^{3+} substitution of a nearby Sn^{2+} ion, respectively. To demonstrate the electronic properties of perovskite without and with SbF_3 passivation, density of states (DOS) of two perovskite supercells was simulated as shown in Figure S19c (Supporting Information). The presence of V_I induces deep trap states energetically situated near the mid-bandgap. When an Sb^{3+} ion is introduced to replace a neighboring Sn^{2+} near the V_I site, the deep-level trap state moves to the valence band edge, indicating the successful conversion to a shallow-level trap state with Sb^{3+} passivation. This passivation is

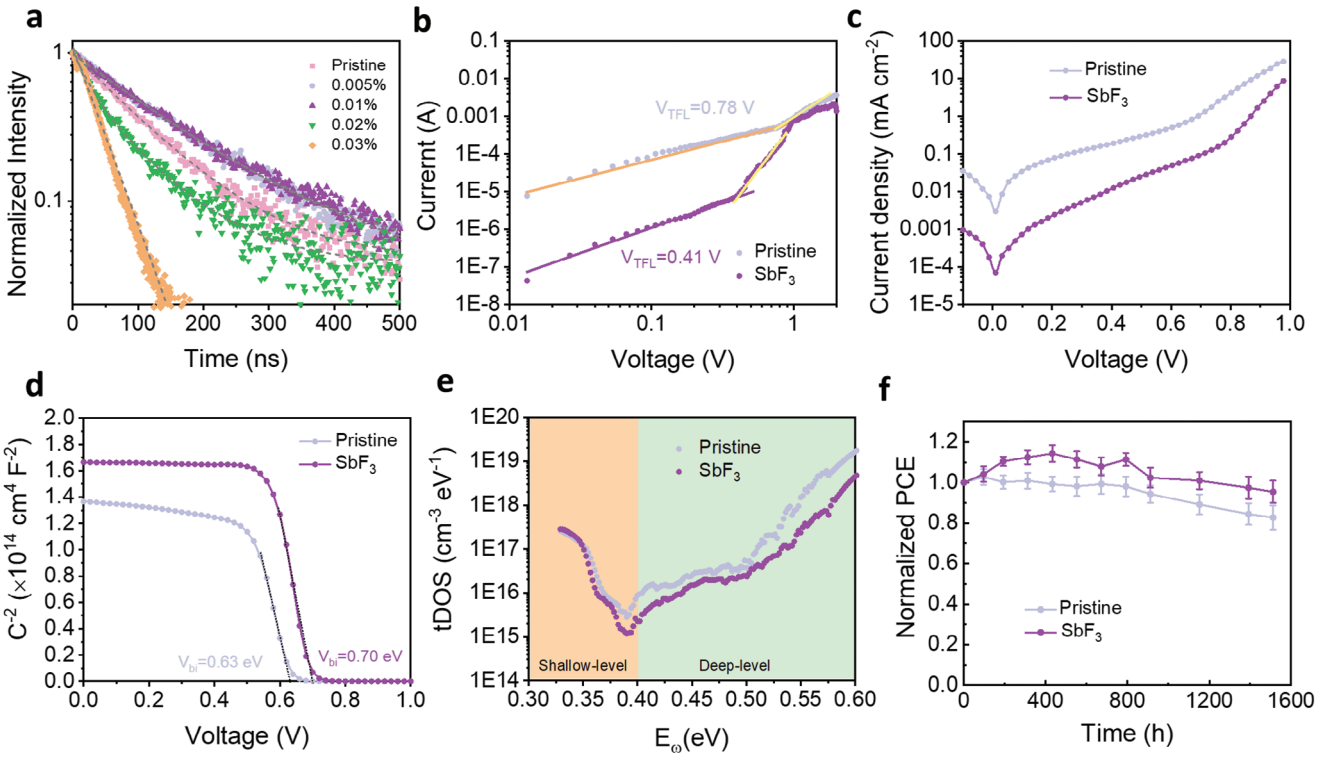

Figure 4. a) Time-resolved PL spectra of the pristine and SbF_3 doped perovskite films with varied concentrations deposited on quartz substrates. b) I–V curves of corresponding electron-only devices. c) Dark *J-V* curves of corresponding PSCs. d) Mott–Schottky plot analysis. e) tDOS curves obtained through admittance spectroscopy of PSCs. f) Long-term stability of the pristine and SbF_3 doped devices stored in N_2 filled glovebox.

beneficial for extending carrier lifetimes and transport properties in perovskite films, further justifying the enhanced performance of resultant PSCs.

Finally, the stability of the unencapsulated PSCs was monitored when they were stored in the N_2 atmosphere and measured in ambient conditions at specific time intervals. As shown in Figure 4f, the pristine devices show an overall downward trend of the evolution of PCE, which finally degrade to 82% of the initial PCE for 1500 h storage. In comparison, SbF_3 doped devices show a gradual increase of efficiency for the initial 900 h and retain 95% of the original efficiency at the same time scale. It is speculated that the generation of Sn^{2+} vacancies can capture and annihilate carriers, thus leading to the degradation of device performance.[50] However, for the SbF_3 doped devices, abundant Sb^{3+} at the grain boundaries will diffuse into the perovskite grains with Sn^{2+} vacancies due to its lower formation energy as indicated by our DFT calculations, which will further counter-dope the perovskite layer and consequently lead to the increase of device efficiency tentatively.

3. Conclusions

In summary, we find that the introduction of Sb^{3+} can effectively counter-dope the oxidized Sn-based perovskites and improve the carrier mobility, carrier lifetime and eliminate some trap states, leading to a substantial enhancement of the V_{OC} and FF of the Sn-based PSCs. As a result, target devices deliver a PCE of 14.37% accompanied by a high V_{OC} of 0.938 V, and also an elongated lifespan, with a 95% PCE retention after 1500 h of storage in a nitrogen atmosphere. This work presents a new insight into the counter-doping effect of Sn-based perovskite with the introduction of trivalent cations and highlights the significance of eliminating p-doping in the perovskite layer for developing high-performance Sn-based PSCs.

Supporting Information

Supporting Information is available from the Wiley Online Library or from the author.

Acknowledgements

T.Y.W. and H.L.L. contributed equally to this work. This work is supported by the Research Grants Council of Hong Kong, China (Project No. 15306822 and C1009-17EF), and the Hong Kong Polytechnic University, Hong Kong, China (ZE2X). This work is also supported by Shenzhen Science and Technology Innovation Commission (Project No. SGDX20210823103401011).

Conflict of Interest

The authors declare no conflict of interest.

Data Availability Statement

The data that support the findings of this study are available in Supporting Information of this article.

Keywords

counter-doping, efficiency, Sn-based perovskite solar cell, trivalent antimony

Received: February 27, 2024
Revised: May 13, 2024
Published online: May 21, 2024

[1] A. Kojima, K. Teshima, Y. Shirai, T. Miyasaka, *J. Am. Chem. Soc.* **2009**, *131*, 6050.
[2] C. Fei, N. Li, M. Wang, X. Wang, H. Gu, B. Chen, Z. Zhang, Z. Ni, H. Jiao, W. Xu, Z. Shi, Y. Yan, J. Huang, *Science* **2023**, *380*, 823.
[3] Best Research-Cell Efficiencies, https://www.nrel.gov/pv/cell-efficiency.html, (accessed: June 2023).
[4] X. Yu, D. Gao, Z. Li, X. Sun, B. Li, Z. Zhu, Z. a. Li, *Angew. Chem.* **2023**, *135*, e202218752.
[5] X. Liu, B. Zheng, L. Shi, S. Zhou, J. Xu, Z. Liu, J. S. Yun, E. Choi, M. Zhang, Y. Lv, W.-H. Zhang, J. Huang, C. Li, K. Sun, J. Seidel, M. He, J. Peng, X. Hao, M. Green, *Nat. Photonics* **2023**, *17*, 96.
[6] Z. Li, X. Sun, X. Zheng, B. Li, D. Gao, S. Zhang, X. Wu, S. Li, J. Gong, J. M. Luther, Z. A. Li, Z. Zhu, *Science* **2023**, *382*, 284.
[7] T. Wu, X. Liu, X. Luo, X. Lin, D. Cui, Y. Wang, H. Segawa, Y. Zhang, L. Han, *Joule* **2021**, *5*, 863.
[8] M. Lyu, J. H. Yun, P. Chen, M. Hao, L. Wang, *Adv. Energy Mater.* **2017**, *7*, 1602512.
[9] M. Ren, X. Qian, Y. Chen, T. Wang, Y. Zhao, *J. Hazard. Mater.* **2022**, *426*, 127848.
[10] Z. Xiao, Z. Song, Y. Yan, *Adv. Mater.* **2019**, *31*, 1803792.
[11] J. Cao, F. Yan, *Energy Environ. Sci.* **2021**, *14*, 1286.
[12] A. Abate, *ACS Energy Lett.* **2023**, *8*, 1896.
[13] X. Jiang, H. Li, Q. Zhou, Q. Wei, M. Wei, L. Jiang, Z. Wang, Z. Peng, F. Wang, Z. Zang, K. Xu, Y. Hou, S. Teale, W. Zhou, R. Si, X. Gao, E. H. Sargent, Z. Ning, *J. Am. Chem. Soc.* **2021**, *143*, 10970.
[14] B. B. Yu, Z. Chen, Y. Zhu, Y. Wang, B. Han, G. Chen, X. Zhang, Z. Du, Z. He, *Adv. Mater.* **2021**, *33*, 2102055.
[15] G. Liu, Y. Zhong, W. Feng, M. Yang, G. Yang, J. X. Zhong, T. Tian, J. B. Luo, J. Tao, S. Yang, X. Wang, L. Tan, Y. Chen, W. Wu, *Angew. Chem.* **2022**, *134*, e202209464.
[16] Z. Zhang, M. A. Kamarudin, A. K. Baranwal, G. Kapil, S. R. Sahamir, Y. Sanehira, M. Chen, L. Wang, Q. Shen, S. Hayase, *Angew. Chem.* **2022**, *134*, e202210101.
[17] J. Zhou, M. Hao, Y. Zhang, X. Ma, J. Dong, F. Lu, J. Wang, N. Wang, Y. Zhou, *Matter* **2022**, *5*, 683.
[18] C. Sun, P. Yang, Z. Nan, C. Tian, Y. Cai, J. Chen, F. Qi, H. Tian, L. Xie, L. Meng, Z. Wei, *Adv. Mater.* **2023**, *35*, 2205603.
[19] C. H. Kuan, R. Balasaravanan, S. M. Hsu, J. S. Ni, Y. T. Tsai, Z. X. Zhang, M. C. Chen, E. W. G. Diau, *Adv. Mater.* **2023**, *35*, 2300681.
[20] G. Liu, X. Jiang, W. Feng, G. Yang, X. Chen, Z. Ning, W. Q. Wu, *Angew. Chem., Int. Ed.* **2023**, *62*, e202305551.
[21] Z. Zhang, Y. Huang, C. Wang, Y. Jiang, J. Jin, J. Xu, Z. Li, Z. Su, Q. Zhou, J. Zhu, R. He, D. Hou, H. Lai, S. Ren, C. Chen, X. Gao, T. Shi, W. Hu, F. Fu, P. Gao, D. Zhao, *Energy Environ. Sci.* **2023**.
[22] D. Song, H. Li, Y. Xu, Q. Yu, *ACS Energy Lett.* **2023**, *8*, 3280.
[23] Y. Su, J. Yang, H. Rao, Y. Zhong, W. Sheng, L. Tan, Y. Chen, *Energy Environ. Sci.* **2023**, *16*, 2177.
[24] X. Zhang, S. Wang, W. Zhu, Z. Cao, A. Wang, F. Hao, *Adv. Funct. Mater.* **2022**, *32*, 2108832.
[25] M. Konstantakou, T. Stergiopoulos, *J. Mater. Chem. A* **2017**, *5*, 11518.
[26] Q. Tai, X. Guo, G. Tang, P. You, T. W. Ng, D. Shen, J. Cao, C. K. Liu, N. Wang, Y. Zhu, C. S. Lee, F. Yan, *Angew. Chem., Int. Ed.* **2019**, *58*, 806.
[27] Z. Zhang, Y. Huang, J. Jin, Y. Jiang, Y. Xu, J. Zhu, D. Zhao, *Angew. Chem.* **2023**, *135*, e202308093.
[28] J. Liu, H. Yao, S. Wang, C. Wu, L. Ding, F. Hao, *Adv. Energy Mater.* **2023**, *13*, 2300696.
[29] T. Wang, Q. Tai, X. Guo, J. Cao, C.-K. Liu, N. Wang, D. Shen, Y. Zhu, C.-S. Lee, F. Yan, *ACS Energy Lett.* **2020**, *5*, 1741.
[30] V. J. Y. Lim, A. M. Ulatowski, C. Kamaraki, M. T. Klug, L. M. Perez, M. B. Johnston, L. M. Herz, *Adv. Energy Mater.* **2023**, *13*, 2200847.
[31] J. Zhang, Y. Zhong, *Angew. Chem., Int. Ed.* **2022**, *61*, e202212002.
[32] R. L. Milot, G. E. Eperon, T. Green, H. J. Snaith, M. B. Johnston, L. M. Herz, *J. Phys. Chem. Lett.* **2016**, *7*, 4178.
[33] R. L. Milot, M. T. Klug, C. L. Davies, Z. Wang, H. Kraus, H. J. Snaith, M. B. Johnston, L. M. Herz, *Adv. Mater.* **2018**, *30*, 1804506.
[34] C. Li, Z. Song, D. Zhao, C. Xiao, B. Subedi, N. Shrestha, M. M. Junda, C. Wang, C. S. Jiang, M. Al-Jassim, R. J. Ellingson, N. J. Podraza, K. Zhu, Y. Yan, *Adv. Energy Mater.* **2019**, *9*, 1803135.
[35] G. Nasti, A. Abate, *Adv. Energy Mater.* **2020**, *10*, 1902467.
[36] J. T.-W. Wang, Z. Wang, S. Pathak, W. Zhang, D. W. deQuilettes, F. Wisnivesky-Rocca-Rivarola, J. Huang, P. K. Nayak, J. B. Patel, H. A. M. Yusof, *Energy Environ. Sci.* **2016**, *9*, 2892.
[37] E. W.-G. Diau, E. Jokar, M. Rameez, *ACS Energy Lett.* **2019**, *4*, 1930.
[38] J. Pascual, M. Flatken, R. Félix, G. Li, S. H. Turren-Cruz, M. H. Aldamasy, C. Hartmann, M. Li, D. Di Girolamo, G. Nasti, A. Abate, *Angew. Chem., Int. Ed.* **2021**, *60*, 21583.
[39] N. Li, S. Tao, Y. Chen, X. Niu, C. K. Onwudinanti, C. Hu, Z. Qiu, Z. Xu, G. Zheng, L. Wang, Q. Chen, H. Zhou, *Nat. Energy* **2019**, *4*, 408.
[40] M. H. Kumar, S. Dharani, W. L. Leong, P. P. Boix, R. R. Prabhakar, T. Baikie, C. Shi, H. Ding, R. Ramesh, M. Asta, M. Graetzel, S. G. Mhaisalkar, N. Mathews, *Adv. Mater.* **2014**, *26*, 7122.
[41] H. W. Qiao, S. Yang, Y. Wang, X. Chen, T. Y. Wen, L. J. Tang, Q. Cheng, Y. Hou, H. Zhao, H. G. Yang, *Adv. Mater.* **2019**, *31*, 1804217.
[42] N. K. Noel, S. N. Habisreutinger, A. Pellaroque, F. Pulvirenti, B. Wenger, F. Zhang, Y.-H. Lin, O. G. Reid, J. Leisen, Y. Zhang, S. Barlow, S. R. Marder, A. Kahn, H. J. Snaith, C. B. Arnold, B. P. Rand, *Energy Environ. Sci.* **2019**, *12*, 3063.
[43] S. Xiong, Z. Hou, S. Zou, X. Lu, J. Yang, T. Hao, Z. Zhou, J. Xu, Y. Zeng, W. Xiao, W. Dong, D. Li, X. Wang, Z. Hu, L. Sun, Y. Wu, X. Liu, L. Ding, Z. Sun, M. Fahlman, Q. Bao, *Joule* **2021**, *5*, 467.
[44] Y.-N. Lu, J.-X. Zhong, Y. Yu, X. Chen, C.-Y. Yao, C. Zhang, M. Yang, W. Feng, Y. Jiang, Y. Tan, L. Gong, X. Wei, Y. Zhou, L. Wang, W.-Q. Wu, *Energy Environ. Sci.* **2021**, *14*, 4048.
[45] C. C. Stoumpos, C. D. Malliakas, M. G. Kanatzidis, *Inorg. Chem.* **2013**, *52*, 9019.
[46] J. Xu, A. Maxwell, M. Wei, Z. Wang, B. Chen, T. Zhu, E. H. Sargent, *ACS Energy Lett.* **2021**, *6*, 4220.
[47] Y.-T. Huang, S. R. Kavanagh, D. O. Scanlon, A. Walsh, R. L. Hoye, *Nanotechnology* **2021**, *32*, 132004.
[48] B. Yang, D. Bogachuk, J. Suo, L. Wagner, H. Kim, J. Lim, A. Hinsch, G. Boschloo, M. K. Nazeeruddin, A. Hagfeldt, *Chem. Soc. Rev.* **2022**, *51*, 7509.
[49] G. Kim, H. Min, K. S. Lee, D. Y. Lee, S. M. Yoon, S. I. Seok, *Science* **2020**, *370*, 108.
[50] C. Wang, F. Gu, Z. Zhao, H. Rao, Y. Qiu, Z. Cai, G. Zhan, X. Li, B. Sun, X. Yu, B. Zhao, Z. Liu, Z. Bian, C. Huang, *Adv. Mater.* **2020**, *32*, 1907623.